Research Square

Preprints are preliminary reports that have not undergone peer review.
They should not be considered conclusive, used to inform clinical practice,
or referenced by the media as validated information.

Exploring Rosemary Essential Oil as an Eco-Friendly Corrosion Inhibitor for low-alloy Steel in 1 M H2SO4: Electrochemical Studies, Weight Loss, and Computational insights

WAFAA ZRIOUEL

wafaa.zriouel-etu@etu.univh2c.ma

Laboratory of Engineering and Materials (LIMAT), Faculty of Sciences Ben M'sick, University Hassan II of Casablanca, Morocco https://orcid.org/0000-0003-1510-7057

Hassan MABRAK

Information Processing Laboratory (IPL), Faculty of Sciences Ben M'sick, University Hassan II of Casablanca, Morocco

Mohammed OUBAHOU

Information of Processing Laboratoty (IPL), Faculty of Sciences Ben M'sick, University Hassan II of Casablanca, Morocco

Youssef Ghandi

Laboratory of Physical-Chemistry of Applied Materials (LCPMA), Faculty of Sciences Ben M'sick, University Hassan II of Casablanca, Morocco

Youssef Naimi

Information Processing Laboratory (IPL), Faculty of Sciences Ben M'sick, University Hassan II of Casablanca, Morocco

Belkheir HAMMOUTI

Euro-Mediterranean University of Fes: Universite Euro-Mediterraneenne de Fes

Research Article

Keywords: Corrosion inhibition, Essential oil, adsorption, Langmuir, DFT

Posted Date: February 24th, 2026

DOI: https://doi.org/10.21203/rs.3.rs-8704414/v1

License: This work is licensed under a Creative Commons Attribution 4.0 International License.
Read Full License

Abstract

This work explores the potential of rosemary essential oil (REO) as an environmentally friendly corrosion inhibitor for low-alloy steel in 1 M H_2SO_4. The chemical composition of the oil, dominated by eucalyptol and α-pinene, was first established by GC-FID analysis. The inhibitory performance of REO was evaluated using gravimetric measurements, potentiodynamic polarization, electrochemical impedance spectroscopy, and temperature-dependent tests. These experiments consistently showed that REO reduces the corrosion rate by forming a protective layer on the steel surface, with optimal performance observed at 1.5 g/L. The decrease in corrosion current density, the widening of the Nyquist loops, and the reduction in double layer capacitance confirm the progressive coverage of the surface achieved by the active constituents of the oil. Thermodynamic and kinetic parameters further indicate that the inhibitor increases the energy barrier of the corrosion reaction and maintains good stability at high temperatures. Adsorption studies have revealed that REO constituents follow a Langmuir adsorption model and exhibit spontaneous adsorption due to a strong affinity with the metal surface. Additional DFT calculations, molecular electrostatic potential (MEP) analyses, and Monte Carlo simulations highlight the predominant role of oxygenated monoterpenes, particularly eucalyptol, isoborneol, and terpineols in stabilizing the organic film through electron-donating interactions.

Introduction

Low Alloy Steel (LAS) is a widely employed material in construction, storage, and engineering, valued for its cost efficiency, availability, and ease of fabrication. Its mechanical properties make it a suitable choice for diverse industrial and manufacturing applications (Rajeev et al, 2017; Khan et al, 2018). The corrosion of low alloy steel in acidic environments presents a major challenge across various industrial sectors, including petroleum refining, chemical processing, and marine engineering. The deterioration of metal surfaces due to aggressive corrosive media results in significant economic losses and safety risks. Traditional corrosion inhibitors (organic and inorganic compounds with heteroatoms) present toxicity risks and a significant environmental impact (Aoudj et al, 2022). To address this, several research projects have been conducted in recent years to develop and study green corrosion inhibitors. Essential oils and plant extracts offer a promising alternative for corrosion inhibition, providing a sustainable and environmentally friendly solution due to their biodegradability and rich composition of bioactive compounds (Mahmoud et al, 2025). Previous studies have demonstrated the effectiveness of various natural substances in mitigating corrosion, such as Aloe Vera (Mahmoud et al, 2025), Geranium essential oil (Zriouel et al, 2025), Ballota hirsuta essential oil (Ou-Ani et al, 2025) and others, highlighting their potential as eco-friendly alternatives to traditional inhibitors. Among these natural inhibitors, rosemary essential oil (REO) has attracted growing interest due to its diverse benefits, including its antidepressant effects (Niu et al, 2025), insecticidal activity (Aulicky et al, 2025), antimicrobial and antioxidant properties (Brandt et al, 2023), biological activities, its application in food preservation (Yang et al, 2023), and its potential for corrosion mitigation (Al Jahdaly et al, 2023). REO is rich in bioactive compounds such as α-pinene, 1,8-cineole, camphor, and borneol, known for their strong antioxidant and antimicrobial properties. These compounds contain oxygenated functional groups that promote adsorption onto metal surfaces, forming a protective barrier against corrosive agents. Additionally, its complex composition, consisting of monoterpenes and oxygenated terpenoids, enhances its inhibition

efficiency by facilitating strong interactions with the steel surface and blocking active corrosion sites. This study aims to evaluate the inhibitory performance of REO on the corrosion of low alloy steel. The inhibition efficiency of REO was assessed using potentiodynamic polarization, electrochemical impedance spectroscopy, and weight loss measurements, complemented by molecular dynamics and Monte Carlo simulations to gain deeper insights into its adsorption behavior and protective mechanisms.

1. Materials and methods

1.1 Low Alloy Steel (LAS) composition and aggressive solution

Table 1
Low Alloy Steel composition

Elements	**C**	**Si**	**Mn**	**P**	**S**	**Cr**	**Mo**	**Ni**	**Nb**	**Al**
Percentage	0.300	0.468	0.627	0.015	0.017	0.251	0.030	0.091	0.006	0.020
Elements	**Cu**	**Co**	**B**	**Ti**	**V**	**W**	**Sn**	**Ca**	**Ce**	**La**
Percentage	0.250	0.006	0.001	0.016	0.004	0.008	0.010	0.001	< 0.002	< 0.005
Elements	**Mg**	**Pb**	**As**	**Sb**	**Zn**	**Zr**	**Te**	**Fe**		
Percentage	0.003	0.007	0.059	0.023	< 0.005	< 0.001	0.017	97.762		

The corrosive solution used for all experiments was 1 M H_2SO_4, prepared by appropriate dilution of concentrated analytical-grade sulfuric acid (97%) supplied by Sigma-Aldrich.

1.2 Rosemary Essential oil: plant and characterization

The essential oil used in this study was obtained from *Rosmarinus officinalis* cineoliferum (CT cineole), commonly referred to as rosemary (cineole). The plant material consisted of flowering tops harvested from wild populations thriving in the Mediterranean garrigues of the Maghreb region, an area well recognized for producing high-quality rosemary essential oil. Harvesting was carried out during the optimal flowering season, under favorable climatic conditions that enhance the biosynthesis of aromatic compounds. The essential oil was extracted by complete steam distillation of the flowering tops. Yields reported in the literature for *Rosmarinus officinalis* cineoliferum typically range between 1.0% and 2.0% (w/w), depending on the origin and harvesting period. The resulting product is a Chemotyped Essential Oil (HECT), ensuring botanical authentication, chemical traceability, and consistent quality.

The characterization of Rosemary Essential Oil (REO) was performed using gas chromatography (GC) on a Clarus 580 PerkinElmer system equipped with a flame ionization detector (FID). A RESTEK column (60m×0.25 mm ID×0.25 µm) was utilized for the separation.

1.3 Corrosion test

The corrosion behavior of REO was investigated using two electrochemical techniques, potentiodynamic polarization and electrochemical impedance spectroscopy (EIS). All measurements were carried out using a Voltalab PGZ100 electrochemical workstation controlled by Voltamaster 4 software. The experiments were performed in an electrochemical cell equipped with a standard three-electrode configuration. The Low Alloy Steel, described above, served as the working electrode (WE), a platinum electrode with a surface area of 0.4 cm^2 was used as the counter electrode (CE), while a saturated Ag/AgCl electrode functioned as the reference electrode (RE). Before each electrochemical measurement, the working electrode was first immersed in the test solution and held at its open circuit potential (OCP) for 30 minutes to ensure the stabilization of the electrochemical system. Electrochemical impedance spectroscopy was then carried out using a sinusoidal perturbation of 10 mV amplitude, over a frequency range from 100 kHz to 10 mHz. The impedance data were fitted and analyzed using EC-Lab software. Potentiodynamic polarization curves were recorded immediately after EIS, at a scan rate of 1 mV/s, over a potential range from −800 mV to − 200 mV vs. Ag/AgCl, covering the corrosion potential. All measurements were conducted at a controlled temperature of 298 K.

1.4 Gravimetric test

Gravimetric corrosion measurements were carried out in accordance with ASTM G31-72. Weight-loss coupons (1.4 cm × 0.5 cm × 0.5 cm), prepared as described above, were carefully cleaned, dried, and weighed (m_0) before exposure. Each specimen was immersed in 100 mL of 1.0 M H_2SO_4 at 298 K for 3 h, either without inhibitor (blank) or in the presence of REO at four concentrations (0.5, 1.0, 1.5, and 2.0 g/l) to assess inhibition performance. After immersion, coupons were retrieved, rinsed, chemically cleaned to remove corrosion products, dried and reweighed (W_1). The mass loss was calculated as $\Delta W = W_0 - W_1$.

From the mass-loss data, the corrosion rate (C_R), inhibition efficiency (%IE), and surface coverage (θ) were determined using standard expressions (Oubahou et al, 2025):

$$C_R = \frac{\Delta W}{At}$$

1

$$\theta = \frac{C_{R,Blank} - C_{R,inh}}{C_{R,Blank}}$$

2

$$\%\,IE = \frac{C_{R,Blank} - C_{R,inh}}{C_{R,Blank}} \times 100$$

3

ΔW denotes the mass loss (g), A the exposed area (cm^2), and t the exposure time (h). Here, $C_{R,Blank}\ and\ C_{R,inh}$ are the corrosion rates measured in the uninhibited and REO-containing solutions, respectively. These definitions enable a quantitative comparison of mass loss and a robust assessment of the REO's corrosion-inhibition efficacy under the specified conditions.

1.5 Computational study

In our previous work (Zriouel et al, 2026), the descriptors of reactivity and the Mulliken atomic charges of all the molecules of rosemary essential oil (REO) were calculated using Density Functional Theory (DFT) with the Dmol module of the Materials Studio software (Delley, 2000). In the present study, to achieve a comprehensive description of electron localization, we extend our investigation by calculating the Molecular Electrostatic Potential (MEP) using DFT optimization at the B3LYP/cc-pVDZ level of theory in the Gaussian 09W software program (Radek, 2009) and the construction and visualization of the various molecules were carried out using GaussView6.0 (Dennington et al, 2016). In addition, the adsorption behavior of all REO molecules was investigated by means of Monte Carlo simulations, carried out with the Adsorption Locator module of the Materials Studio software in both aqueous and gas phases, to provide deeper insight into their interaction with metallic surfaces.

2. Results and outcomes

2.1 Chemical composition of REO

The characterization of REO, presented in Table 2, reveals a molecular profile dominated by eucalyptol (49.01%) and α-pinene (17.31%) as the most abundant constituents. Eucalyptol, a highly oxygenated monoterpene, contributes significantly to the oil's polarity and enhances its ability to interact with metallic surfaces through electrostatic interactions and potential hydrogen bonding, thereby reinforcing corrosion inhibition (Nagarajan et al, 2023). The second dominant constituent of REO is α-pinene (17.31%), a hydrophobic terpene capable of adsorbing onto metallic surfaces through π–electron interactions and van der Waals forces, thereby complementing the action of oxygenated components. Despite its known risks to human health and the environment, α-pinene has found applications in controlling waste gas emissions, highlighting its potential economic and environmental advantages, and its significant concentration in REO suggests that its contribution to corrosion inhibition should not be overlooked (Zarei et al, 2024; Zhou et al, 2023; Charrad et al, 2022). Other notable molecules, including camphene (3.75%), isoborneol (3.82%), terpineol (3.25%), and α-terpineol (2.47%), provide additional polar functional groups (hydroxyl or ether moieties), which facilitate adsorption and promote the formation of a protective barrier. The presence of sesquiterpenes such as β-caryophyllene (6.42%) and humulene (0.76%) suggests that nonpolar hydrocarbons may also contribute to surface coverage, improving the compactness and stability of the adsorbed film. Taken together, this molecular distribution indicates that REO likely inhibits corrosion via a mixed adsorption mechanism, involving both physisorption (through weak van der Waals forces) and chemisorption (through electronic interactions of oxygenated groups with LAS atoms) (Okafor et, 2024; Peköz et al, 2016). The predominance of oxygenated monoterpenes, particularly eucalyptol, underscores the potential of REO as an effective green corrosion inhibitor, capable of forming a stable and protective layer on metallic surfaces.

Table 2
Chemical composition of REO obtained by GC-FID

Molecule	Percentage %	Molecule	Percentage %
Alpha-Thujene	0.53	Beta-thujene	0.26
Alpha-pinene	17.31	Terpinolene	0.87
Camphene	3.75	Eucalyptol	49.01
Beta- myrcene	1.81	Gamma-terpinene	1.39
O-cymene	0.77	Alpha-terpinolene	0.51
Linalool	1.01	Isoborneol	3.82
Terpinen-4-ol	0.8	Terpineol	3.25
Borneol acetate	1.15	Beta-caryophyllene	6.42
Humulene	0.76	Gamma-cadinene	0.81
Alpha-terpineol	2.47		

2.2 Gravimetric Analysis and Discussion

The corrosion behaviour of LAS in 1 M H_2SO_4 solution was evaluated through weight-loss measurements in the absence and presence of different concentrations of REO, as presented in Table 3. After 3 h of immersion at 298 K, the mass loss of each specimen was determined as the difference between its initial and final weights, and these values were used to calculate the corrosion rate (CR), surface coverage (θ), and inhibition efficiency (%IE). The obtained results are summarized in Table 1. The data clearly demonstrate that the introduction of REO significantly decreases the corrosion rate, confirming its strong protective effect against acid attack. In the uninhibited medium, the corrosion rate reaches its highest value (1.313×10^{-2} g h^{-1} cm^{-2}), indicating considerable metal dissolution. As the inhibitor concentration increases, the corrosion rate progressively declines, attaining its lowest value (1.43×10^{-3} g h^{-1} cm^{-2}) at 1.5 g/l, which corresponds to the highest inhibition efficiency (89.10%). This pronounced reduction in metal loss suggests that REO molecules effectively adsorb onto the alloy surface, forming a compact protective layer that limits the access of aggressive ions. A slight increase in corrosion rate at 2 g·L^{-1} ($CR = 2.84 \times 10^{-3}$ g h^{-1} cm^{-2}, IE = 78.37%) indicates that beyond the optimal concentration, the adsorption sites may become saturated, and excess inhibitor could disturb the uniform protective film. Such behaviour is typical of adsorption-controlled inhibition mechanisms, where multilayer formation or weakly bound species can reduce the overall protection efficiency (Denisa-Ioana et al, 2025). Generally, REO exhibits remarkable corrosion-inhibiting ability for LAS in acidic media, with an optimal performance at 1.5 g/l, yielding the highest inhibition efficiency (89.10%) and the lowest corrosion rate (1.43×10^{-3} g h^{-1} cm^{-2}). These findings confirm the strong surface-blocking and adsorption capacity of REO under the studied conditions.

Table 3
C_R in (g h-1 cm-2) θ, and %IE data obtained from WL tests for LAS in acidic solutions with and without different concentration of REO at 25◦C.

Inhibitor concentration	\varvecΔW (g)	C_R (g $h^{-1}cm^{-2}$)	\varvecθ	IE (%)
Blank	0.1298	0.01313	-	-
0.5	0.0721	0.00729	0.4343	43.43
1	0.0315	0.00318	0.7523	75.23
1.5	0.0142	0.00143	0.8910	89.10
2	0.0281	0.00284	0.7837	78.37

2.3 OCP curves

The evolution of the open circuit potential (OCP) of Low Alloy Steel immersed in 1 M H_2SO_4, in the absence and presence of REO at various concentrations, is displayed in Fig. 1.

OCP monitoring over time provides insight into the stability of the electrochemical interface and the initial adsorption behavior of the inhibitor on the metal surface. In the uninhibited solution, the potential stabilizes rapidly at approximately − 430 mV vs Ag/AgCl, reflecting active dissolution of the steel surface and the absence of any protective film. The nearly steady potential throughout the immersion period indicates that no passivating layer is formed, and the metal remains exposed to the corrosive environment (Bharati et al, 2025). Upon addition of REO, notable shifts in OCP are observed. For the lowest concentration (0.5 g/l), the potential is initially much more negative (~–470 mV) and continues to shift positively over time, approaching the blank value near the end of the immersion. This behavior suggests slow adsorption kinetics at this dosage, where active dissolution dominates at the start but gradually decreases as surface coverage improves. At intermediate concentrations (1.0 g/l, and 1.5 g/l), the OCP values exhibit distinct behavior. Both curves start slightly above or near the blank potential but then undergo an initial positive shift before stabilizing. In particular, the curve for 1.5 g/l of our inhibitor demonstrates a pronounced upward drift, suggesting a more rapid and effective adsorption of REO constituents onto the steel surface. This progressive shift toward less negative potentials indicates a suppression of anodic iron dissolution, which is a typical signature of barrier formation through molecular adsorption (Suhartono et al, 2024, Zouarhi et al, 2023). The relatively stable plateau observed after 1200 seconds further supports the establishment of a protective layer at this concentration. In contrast, the response at the highest concentration (2.0 g/l) reveals a more complex profile. Although it initially starts more negative, the curve quickly shifts positively within the first 400 s, then gradually decreases again toward more negative values. This late-stage drift may reflect surface saturation effects, partial desorption, or competitive displacement of adsorbed molecules. Such destabilization is often associated with excessive inhibitor accumulation, where multilayer formation or micellar structures interfere with cohesive film integrity. It can be clearly concluded from the OCP trend that the interaction between REO molecules and the steel surface is strongly dependent on concentration. Moderate additions (notably 1.5 g/l) promote more stable and less negative potentials, consistent with efficient adsorption and surface coverage. Deviations at lower and higher concentrations, however, point to either insufficient interaction or disruption of protective film formation.

2.4 Polarization method

The potentiodynamic polarization behavior of Low allow steel in 1 M H_2SO_4, with and without REO, is illustrated in Fig. 2, and the corresponding electrochemical parameters are summarized in Table 4. These include the corrosion potential (E_{corr}), anodic (βa) and cathodic (βc) Tafel slopes, corrosion current density (i_{corr}), and the inhibition efficiency (E_{PDP}%) (Zriouel et al, 2026):

$$\% \text{ IE} = \frac{i_{corr} - i\prime_{corr}}{i_{corr}} \times 100$$

4

acid solution without and with the addition of REO at different concentrations 298 K.

In acidic environments, the corrosion of LAS involves two simultaneous electrochemical reactions. The anodic reaction consists of the dissolution of iron to ferrous ions as reflected by Eq. I, whereas the cathodic reaction, in turn, involves the reduction of hydrogen ions to hydrogen gas (Eq. II).

$Fe \rightarrow Fe^{2+} + 2e$ (Eq.I)

$2H + + 2e \rightarrow H$ (Eq.II)

Table 4
Electrochemical parameters derived from PDP tests for LAS/H_2SO_4 with and without the addition of different concentrations of REO

Medium	V (g/l)	-E_{corr}(mv)	I_{corr}(mA/cm^2)	β_a	-β_c	E_{PDP}%
1M H_2SO_4 Blanc	-	412.5	2.75	140.2	158.7	-
REO	0. 5	431.9	1.70	68.4	163.9	37.98
	1	432.5	1.21	58.7	152.8	56.00
	1.5	436.6	0.46	36.7	120.8	83.36
	2	436.0	0.85	52.7	148.3	69.13

Inhibitors can influence the corrosion process by interfering with the anodic reaction, the cathodic reaction, or both, depending on their adsorption behavior and molecular structure. In the absence of the inhibitor, the steel surface displayed a corrosion potential of − 412.5 mV and a high corrosion current density (i_{corr}) of 2.75 mA/cm2, indicating rapid metal dissolution. Upon the addition of REO at various concentrations, there was a noticeable decrease in i_{corr}, reaching a minimum of 0.46 mA/cm^2 at 1.5 g/l. This corresponds to the highest inhibition efficiency of 83.36%. However, at 0.2 g/l, the corrosion current increased slightly to 0.8475 mA/cm, leading to a reduction in inhibition efficiency to 69.13%, possibly due to multilayer formation or desorption phenomena at higher concentrations. The changes in E_{corr} values were relatively modest, with a maximum positive shift of around 24 mV. According to the ± 85 mV criterion widely reported in the literature, such a slight variation indicates that the inhibitor does not preferentially affect only one of the partial corrosion reactions (Nikhil et al, 2026). Therefore, REO appears to influence both the anodic metal dissolution

and cathodic hydrogen evolution processes to a comparable extent. This behavior is further supported by the variations in both anodic and cathodic Tafel slopes. Such trends indicate that the inhibitor's mode of action involves physical or chemical adsorption onto active corrosion sites, reducing the available surface area for charge transfer. The pronounced decrease in i_{corr} with increasing inhibitor concentration up to an optimum level suggests the formation of a protective film on the steel surface. This barrier likely results from the adsorption of active constituents in REO, such as Eucalyptol, Isoborneol and Terpineol, which possesses electron-rich functional groups (–OH, $–OCH_3$) capable of interacting with vacant d-orbitals of iron atoms.

2.5 Effect of temperature and kinetic parameters

Although some inhibitors show excellent efficiency at low temperatures, their performance often deteriorates as the temperature increases. For this reason, the effect of temperature on the inhibition performance of REO was evaluated to assess its stability under more aggressive thermal conditions. As is well known, temperature is a critical parameter that can significantly influence both the corrosion rate and the adsorption behavior of inhibitors. In general, increasing the temperature tends to accelerate the corrosion process by enhancing the dissolution rate of metal and the mobility of ions in solution, and it can also lead to desorption of inhibitor molecules from the metal surface (Priya, et al, 2023). Based on Fig. 3 and the data presented in Table 5, it is evident that the corrosion current density (i_{corr}) of LAS in uninhibited medium increased significantly with temperature, rising from 0.46 mA/cm^2 at 298 K to 1.33 mA/cm^2 at 328 K. In contrast, in the presence of 0.15 g/l REO, the i_{corr} values were much lower at all temperatures and increased more moderately, from 0.46 mA/cm^2 at 298 K to 1.33 mA/cm^2 at 328 K. This behavior reflects the persistent protective action of the inhibitor despite thermal activation of the corrosion process. In terms of efficiency, the EI (%) slightly decreased with temperature, from 83.36% at 298 K to 51.63% at 328 K. This small drop in efficiency suggests partial desorption of inhibitor molecules at elevated temperatures, a typical behavior when physical interactions contribute to the adsorption mechanism (Li et al, 2022; Zriouel et al, 2025). However, the retention of high efficiency even at 328 K implies that the adsorption of REO involves strong interactions, likely chemical in nature, which confer thermal stability to the protective layer. Thus, REO can be considered a thermally stable and efficient corrosion inhibitor for steel in acidic environments.

Table 5
Electrochemical data of LAS in 1 M H_2SO_4 with and without 1.5 g/l of REO at different temperatures.

Medium	Conc.	T (K)	-E_{corr}(mv)	i_{corr}(mA/cm^2)	β_a	-β_c	EI (%)
1M H_2SO_4	Blank	298	412.5	2.75	140.2	158.7	-
		308	432.2	3.35	108.9	173.5	-
		318	426.5	3.95	146.1	177.8	-
		328	423.2	4.54	136.7	176.9	-
REO	1.5	298	436.6	0,46	36.7	120.8	83,36
		308	455.0	0,81	40.1	111.1	75.86
		318	448.7	1,33	58.0	149.3	66.33
		328	448.2	1,56	34.2	87.1	65.64

To gain insight into the kinetic and thermodynamic aspects of the corrosion process, Arrhenius and transition state equations were applied to the experimental data (Equations 5 and 6), and the corresponding plots are presented in Figs. 4 and 5. The calculated activation energy (E_a), enthalpy (ΔH_a), and entropy (ΔS_a) values are summarized in Table 6.

$$lni_{corr} = \frac{-E_a}{RT} + lnA$$

5

$$i_{corr} = \frac{RT}{Nh} exp\left(\frac{\Delta S_a}{R}\right) exp\left(-\frac{\Delta H_a}{RT}\right)$$

6

The obtained results reveal a clear modification of the corrosion mechanism upon the addition of REO. In the absence of inhibitor, the activation energy of steel dissolution was found to be 13.58 kJ mol^{-1}, whereas the enthalpy and entropy values were 10.98 kJ mol^{-1} and -199.55 J mol^{-1} K^{-1}, respectively. Such a low Ea value reflects the ease of the corrosion process in the uninhibited solution, while the large negative ΔSa indicates a highly ordered activated complex, suggesting that the system is dominated by significant constraints at the transition state. In contrast, the presence of 0.15 g/l of inhibitor markedly increased Ea to 34.00 kJ mol^{-1} and ΔHa to 31.39 kJ mol^{-1}, while ΔSa rose to -145.41 J mol^{-1} K^{-1}. This pronounced increase in Ea demonstrates that the inhibitor raises the energy barrier required for the corrosion reaction to proceed, thereby slowing the dissolution rate of steel (Cherrak et al, 2021). Similarly, the higher ΔHa value confirms the endothermic character of the activation process in the inhibited medium, consistent with the greater energy demand for metal dissolution when the surface is partially covered by inhibitor molecules. Moreover, the less negative ΔSa value reflects a decrease in the degree of order at the transition state, which can be attributed to the replacement of water molecules by inhibitor species at the metal/solution interface, leading to a more disordered activated complex.

Hence, it can be concluded that the addition of REO effectively modifies the energetic pathway of the corrosion process, primarily by increasing the activation energy and reducing the rigidity of the system at the transition state. This behavior can be attributed to the strong adsorption of the inhibitor molecules on the steel surface, which hinders the access of aggressive ions and thereby enhances the stability of the metal against acid attack (Umoren et al, 2013).

Table 6
Thermodynamic activation parameters of the synthesized corrosion inhibitors.

	E_a (KJ/mol)	ΔH_a (KJ/mol)	ΔS_a (J/mol K)
Blank	13.58	10.98	-199.55
$\varvec{R}\varvec{E}\varvec{O}$	34.00	31.40	-145.41

2.6 Impedance study

Electrochemical impedance spectroscopy was employed to further assess the corrosion inhibition performance of REO on low alloy steel (LAS) in 1 M H□SO□ at 298 K. The extracted EIS parameters, in the absence and presence of REO, are summarized in Table 7, while the corresponding Nyquist plots are illustrated in Fig. 6. The inhibition efficiency was calculated from the charge transfer resistance values according to the following equation (Haque et al, 2024):

$$E_{EIS} = \frac{R_{ct} - R_{ct0}}{R_{ct}} \times 100 \quad (7)$$

where R_{ct} et R_{ct0} represent the charge transfer resistance of the steel in the absence and presence of REO, respectively.

In the absence of inhibitor, the Nyquist plot exhibits a single, depressed capacitive semicircle, characteristic of a corrosion process governed by charge transfer at the metal/solution interface. The lack of additional features at low frequencies indicates that no adsorption–desorption or relaxation processes are involved in the blank system, and the steel surface remains directly exposed to the aggressive medium. In contrast, the introduction of REO significantly modifies the impedance response. The diameter of the capacitive loop increases progressively with concentration, pointing to an increase in charge transfer resistance (Rct) and, therefore, a decrease in corrosion rate. In addition, at all tested concentrations of the oil, the Nyquist spectra reveal the emergence of an inductive loop at low frequencies. This feature, absent in the blank solution, is typically associated with surface phenomena such as the relaxation of adsorbed intermediate species or dynamic adsorption–desorption of inhibitor molecules. The appearance of this loop thus confirms the active participation of REO constituents in interfacial processes (Carmona-Hernandez et al, 2025).

To quantitatively interpret these spectra, the impedance data were fitted using the equivalent circuits shown in Fig. 7, and the extracted parameters are listed in Table 7. The circuit comprises the solution resistance (Rs), charge transfer resistance (Rct), polarization resistance (Rp), a constant phase element (CPE) to account for non-ideal capacitive behavior, and an inductive element (L) with its associated resistance (RL) reflecting adsorption-related processes.

The enlargement of the semicircle persists with increasing concentration up to 1.5 g/l, where the maximum diameter is recorded, corresponding to the highest inhibition efficiency (81%). However, further addition to 2g/l leads to a reduction in semicircle size and a decrease in efficiency (58%). One may attribute this decline to the formation of less compact or unstable layers at high concentration, possibly arising from multilayer adsorption or aggregation effects, which hinder uniform surface protection. The above mentioned findings are in full agreement with the polarization results, where the optimum protection was also observed at 1.5 g/l. The close correspondence between Rct and E_{EIS}% across both methods reinforces the conclusion that REO achieves its inhibitive effect by impeding the charge transfer at the metal/electrolyte interface. Moreover, a clear decrease in the CPE values was observed with increasing REO concentration. This reduction in double-layer capacitance is commonly attributed to one or more of the following phenomena:

- A decrease in the local dielectric constant at the interface due to replacement of water molecules by organic constituents of the oil (Zhao et al, 2023).
- A reduction in the exposed metal surface area resulting from adsorbed inhibitor molecules;
- And/or an increase in the thickness of the electrical double layer, due to the formation of an organic film.

Table 7
Electrochemical Behavior and Corrosion Inhibition Efficiency of REO in 1 M H_2SO_4 at Different Concentrations.

C(g/l)	R_s ($\Omega.cm^2$)	R_{ct} ($\Omega.cm^2$)	C_{dl} ($\mu F.cm^{-2}$)	n	L (H.cm^2)	R_L ($\Omega.cm^2$)		IE (%)
Blank	1.01	8.06	29.44	0.89	-	-	-	-
0.5	1.46	24.86	23.52	0.85	11.45	2.82	0.6758	67.578
1	1.33	36.11	15.90	0.73	14.85	2.99	0.7768	77.679
1.5	2.24	44.63	9.51	0.81	21.89	6.41	0.8194	81.940
2	1.52	19.39	6.48	0.85	17.55	3.02	0.5843	58.432

2.7 Adsorption behavior of REO

Understanding how inhibitor molecules interact with the metallic surface is essential to elucidate their corrosion protection mechanism. In this context, adsorption isotherms offer a valuable approach for describing the nature and strength of the interactions between the active species and the steel surface in acidic media. During immersion, both the water molecules and the inhibitor species compete for available adsorption sites on the metal/electrolyte interface. The corrosion inhibition is typically associated with the adsorption of organic molecules, which displace pre-adsorbed water or ions from the steel surface. This process is commonly described by the Bockris–Devanathan–Müller model, which conceptualizes adsorption as a substitution reaction between water molecules at the interface and the inhibitor present in solution:

Org (sol) + xH_2O (ads) → Org (ads) + xH_2O (sol)

In this equation, x represents the number of water molecules replaced by a single inhibitor molecule. The adsorption itself can proceed via different mechanisms depending on the structure and properties of the organic constituents in the REO. These include:

- Electrostatic attraction between charged species and the electrically charged metal surface;
- donor–acceptor interactions involving lone electron pairs on heteroatoms and vacant d-orbitals of the metal;
- π-electron interactions between aromatic rings and the metal surface;
- A combination of these effects.

In order to describe the adsorption behavior of REO on Low alloy steel, the experimental data derived from electrochemical measurements were analyzed using different theoretical adsorption isotherms. Among the most widely used are Langmuir, Temkin, Frumkin, and Frendlich, each providing different assumptions regarding surface homogeneity, molecular interactions, and coverage behavior. These models are expressed by the following equations:

Temkin : $lnC_{inh} = \mathrm{g}\theta \ - lnK_{ads}$ (8)

Frumkin : $log\left[\left(\frac{\theta}{(1-\theta)\times C_{inh}}\right)\right] = logK_{ads} + \mathrm{g}$ (9)

Freundlich

$log\theta \ = \mathrm{n}logC_{inh} + logK_{ads}$ (10)

Langmuir : $\frac{C_{inh}}{\theta} = \frac{1}{K_{ads}} + C_{inh}$ (11)

In the above expressions, C is the inhibitor concentration, θ is the surface coverage degree, K is the adsorption equilibrium constant, and the other parameters relate to interaction strength or number of replaced molecules. The degree of fit to each model offers insights into whether the adsorption is monolayer, involves lateral interactions, or exhibits non-ideal behavior. Among the models tested, the Langmuir isotherm provided the best fit, as evidenced by the linearity of the plot with a slope value of 1.72, which is very close to unity and thus supports the validity of the model. The adsorption equilibrium constant (Kads) was found to be 30.39 L mol^{-1}, highlighting the strong affinity of the inhibitor molecules for the steel surface. Furthermore, the standard free energy of adsorption (ΔG°ads) was calculated to be -35.52 kJ mol^{-1}, which suggests a predominantly physical adsorption process reinforced by electrostatic interactions. Nevertheless, the relatively high magnitude of Kads indicates that the interaction is sufficiently strong to ensure the formation of a stable protective layer. Thus, one may infer that the adsorption of REO molecules follows a predominantly spontaneous and stable interaction with the steel substrate, ensuring effective surface coverage and enhanced resistance against acid-induced corrosion.

It is worth noting, however, that the interpretation of adsorption isotherms is not entirely free from limitations. As highlighted by Kokalj, the assumptions underlying models such as Langmuir may oversimplify the real adsorption scenario, especially when dealing with heterogeneous molecular structures, non-ideal surface coverage, or lateral interactions between adsorbed species. Nevertheless, the good linearity obtained in the present case supports the predominance of

Langmuir-type adsorption, thereby reinforcing the key role of surface coverage in the inhibition process.

Table 8
Langmuir isotherm–based adsorption and thermodynamic parameters of REO on LAS in H_2SO_4.

Inhibitor	K_{ads} (L/mol)	R^2	ΔG_{ads} (kJ/mol)	Slope
$\varvec{R}\varvec{E}\varvec{O}$	30.39	0.92	-35.52	1.72

3. Computational study

3.1. Molecular Electrostatic potential (MEP)

Molecular electrostatic potential (MEP) maps are valuable tools for predicting corrosion inhibition behavior, as they illustrate how molecules interact with metal surfaces. In MEP analysis, different colors are assigned to represent varying electrostatic potential values, with electron density typically decreasing in the order: red > orange > yellow > green > blue (Zriouel et al, 2025; Kamarul Baharin et al, 2025). Regions with high electron density (red zones) on the MEP map, often associated with functional groups such as –OH, –C = O, and –C = C, can donate electrons to the metal's d-orbitals, thereby facilitating chemisorption and forming a protective layer. Molecules with higher electron-donating capacity (localized negative potential) generally exhibit stronger adsorption and greater corrosion inhibition efficiency, while those with low electron density (blue regions) may interact weakly, reducing their effectiveness (Mekha et al, 2025). The MEP and contour surface maps of all molecules constituting REO are listed in Table 9.

Among the REO constituents, Linalool (-8.006×10^{-2} a.u.), Eucalyptol (-7.044×10^{-2} a.u.), Isoborneol (-6.887×10^{-2} a.u.), Terpineol (-6.710×10^{-2} a.u.), and Terpinen-4-ol (-6.606×10^{-2} a.u.) exhibit the most negative electrostatic potentials. Owing to their strong electron-donating capacity, these compounds are expected to play a dominant role in adsorption onto the metal surface, thereby enhancing corrosion inhibition efficiency. The presence of functional groups such as –OH and ether moieties is likely responsible for the localized regions of high electron density observed in their MEP profiles.

In contrast, hydrocarbons including α-Pinene, β-Myrcene, Camphene, γ-Cadinene, and Humulene display comparatively lower negative potential values (approximately -2.6×10^{-2} to -3.4×10^{-2} a.u.). Their MEP maps reveal more uniform charge distributions with fewer localized red zones, indicating weaker interactions with the metal surface and a reduced contribution to overall inhibition efficiency.

Furthermore, sesquiterpenes such as β-Caryophyllene and Humulene exhibit relatively symmetrical charge distributions, which may further limit their adsorption tendencies compared to oxygenated monoterpenes. The incorporation of heteroatoms in oxygenated terpenes (alcohols, ethers, and acetates) appears to be the key factor enhancing their electron-donating ability and, consequently, their adsorption strength.

Taken together, the MEP results suggest that oxygenated monoterpenes (Linalool, Terpineols, Isoborneol, Borneol acetate, and Eucalyptol) represent the principal active constituents responsible for the corrosion inhibition potential of REO, while hydrocarbon components play a secondary role with relatively weaker adsorption. This finding supports the broader consensus that polar functional groups significantly enhance the capacity of natural compounds to interact effectively with metal surfaces.

Monte Carlo simulation

Monte Carlo simulations are widely recognized as a powerful tool for exploring adsorption mechanisms at the molecular level, providing detailed insights into inhibitor–surface interactions that govern corrosion protection efficiency. Their ability to evaluate adsorption energetics makes them particularly valuable for predicting the performance of green corrosion inhibitors. Monte Carlo simulations were carried out for the nineteen constituent molecules of REO, each considered individually as a potential green corrosion inhibitor. In addition, a simulation was carried out including all nineteen molecules within the same simulation cell of dimensions ($a = 60.194$ Å, $b = 60.194$ Å, $c = 35.665$ Å) was performed in both the gas phase and an aqueous phase (water + sulfuric acid).

Adsorption studies were conducted using the Adsorption Locator module in Materials Studio, employing the simulated annealing algorithm with the COMPASS force field. Prior to adsorption calculations, the molecular geometries were fully optimized using the Forcite module.

The energetic parameters used to evaluate the adsorption interactions namely, total energy, adsorption energy, rigid adsorption energy, deformation energy, and the individual adsorption energy per molecule (dEad/dNi) are summarized in Tables 10–12. Representative top and side views of the Fe (110) surface with the adsorbed molecules are presented in Fig. 10.

Table 10
Monte Carlo simulation results of REO in Fe (1 1 0)/ 1 M H_2SO_4

Energy of simulation cell	Gas phase	Aqueous phase
Total energy	-692.684	-11072.34
Adsorption energy	-497.660	-1181.921
Rigid adsorption energy	-507.757	-1246.261
Deformation energy	10.097	64.333

The Monte Carlo simulations were carried out to investigate the adsorption of REO molecules on the Fe (110) surface in both gas and aqueous phases. The total energy values demonstrate that adsorption is more favorable in the aqueous medium compared to the gas phase. The aqueous system shows a significantly lower total energy, which indicates that the presence of water and H□SO□ strongly stabilizes the REO–metal interface. This stabilization likely arises from solvation effects, hydrogen bonding, and electrostatic interactions that enhance the adsorption of REO molecules in the corrosive medium. Adsorption energies for both phases are negative, confirming that the adsorption process is energetically favorable in all cases. However, the aqueous phase

exhibits a much more exothermic adsorption energy (–1181.921 kcal/mol) compared to the gas phase (–497.660 kcal/mol). This marked difference highlights the stronger interaction of REO molecules with the Fe (110) surface when water and H□SO□ are present. Such strong adsorption in the aqueous environment suggests that REO molecules can effectively block active sites on the metal surface, thereby limiting the access of corrosive species and enhancing inhibition efficiency.

The comparison between rigid adsorption energy and adsorption energy provides further insight into the role of molecular deformation during adsorption. In both phases, the rigid adsorption energy is more negative, and the difference corresponds to deformation energy. The gas phase shows minimal deformation (10.1 kcal/mol), whereas in the aqueous phase, the deformation energy is considerably higher (64.3 kcal/mol). This indicates that REO molecules undergo substantial structural rearrangement to optimize their interaction with the Fe (110) surface in the presence of H□SO□ and water.

Overall, the Monte Carlo results reveal that the aqueous phase not only promotes stronger adsorption but also induces structural adaptation of the REO molecules to achieve maximum stabilization at the metal interface. This behavior supports the potential of REO as an effective corrosion inhibitor, as strong and stable adsorption on Fe (110) in acidic aqueous media is a key requirement for protection against corrosion.

Table 11
Individual adsorption energy per molecule (dEad/dNi) obtained by Monte Carlo simulation in both gas and aqueous phases.

Molecule	dEad/dNi (Aqueous Phase)	dEad/dNi (Gas Phase)
Alpha pinene	-23.353	-17.538
isoborneol	-8.031	-18.423
Linalool	-16.119	-39.514
o-cymene	-9.564	-24.590
terpinen-4-ol	-36.358	-33.929
Terpineol	-5.716	-27.566
Terpinolene	-23.326	-18.747
alpha-terpineol	-37.758	-12.476
alpha-terpinolene	-16.693	-32.704
alpha-Thujene	-20.196	-18.116
beta- myrcene	-36.487	-28.095
beta-caryophyllene	-40.136	-38.802
beta-thujene	-21.047	-13.982
borneol acetate	-10.427	-30.034
camphene	-0.792	-24.889
Eucalyptol	-17.362	-24.679
gamma-cadinene	-28.298	-35.581
gamma-terpinene	-18.391	-26.714
humulene	-30.767	-33.233
Water	18,081	-
Sulfuric Acid	-0,856	-

Relatively to Table 8, the calculated individual adsorption energies (dEad/dNi) highlight clear differences in the adsorption behavior of REO molecules on the Fe (110) surface in both gas and aqueous phases. The results indicate that adsorption is generally more favorable in the aqueous phase, where the presence of water and H□SO□ strengthens the interaction between inhibitor molecules and the iron surface. This is reflected in the more negative adsorption energies observed for most molecules in solution compared to the gas phase.

In the aqueous medium, several REO molecules stand out as strong adsorbates. β-caryophyllene (–40.136 kJ/mol), β-myrcene (–36.487 kJ/mol), terpinen-4-ol (–36.358 kJ/mol), α-terpineol (–37.758 kJ/mol), and humulene (–30.767 kJ/mol) show the most negative dEad/dNi values, suggesting strong interactions with the Fe (110) surface. Such strong adsorption implies that these molecules can

effectively cover active surface sites, limiting the access of aggressive H□SO□ ions and thereby providing significant corrosion protection.

On the other hand, certain molecules such as camphene (–0.792 kJ/mol), sulfuric acid (–0.856 kJ/mol), and water (+ 18.081 kJ/mol) display weak or unfavorable adsorption energies. This indicates that the corrosive environment itself does not contribute to surface protection and reinforces the idea that REO molecules are essential for inhibition. Interestingly, some molecules such as linalool (–16.119 kJ/mol) and borneol acetate (–10.427 kJ/mol) adsorb more strongly in the gas phase than in aqueous solution, reflecting how solvation can weaken the direct interaction between these inhibitors and the Fe (110) surface.

Comparing across phases also shows that the adsorption strength of certain molecules shifts depending on the environment. For instance, α-pinene, α-terpinolene, γ-terpinene, and eucalyptol display stronger adsorption in aqueous solution, highlighting their adaptability in acidic media. Meanwhile, molecules such as gamma-cadinene and borneol acetate maintain stronger affinities in the gas phase. These differences demonstrate that not all REO constituents contribute equally to inhibition under realistic corrosive conditions.

Table 12
Monte Carlo simulation results of the molecules constituting REO in gas and aqueous phases

Molecule	Phases	Total energy Kcal/mol	Adsorption energy kJ/mol	Rigid adsorption energy kJ/mol	Deformation energy kJ/mol
Iron (1 1 0) + alpha pinene	Gas phase	-77,818	-77,565	-77,961	0,3955
	Aqueous phase	-1280,665	-311,1263	-316,737	5,6108
Iron (1 1 0) + alpha-thujene	Gas phase	15,263	-69,683	-71,145	1,463
	Aqueous phase	-1283.352	-313,813	-323,781	9,968
Iron (1 1 0) + Beta-myrcene	Gas phase	-97,109	-87,004	-88,252	1,248
	Aqueous phase	-1268.225	-298,686	-308,229	9,543
Iron (1 1 0) + Borneol acetate	Gas phase	-119,344	-93,378	-95,137	1,759
	Aqueous phase	-1258.544	-289,006	-306,463	17,457
Iron (1 1 0) + Beta-thujene	Gas phase	19.706	-64.781	-66.274	1.493
	Aqueous phase	-2188.398	-572.500	-594.116	21.616
Iron (1 1 0) + Beta-Caryophyllene	Gas phase	-104.099	-91.842	-99.641	7.798
	Aqueous phase	-2188.704	-572.807	-592.576	19.769
Iron (1 1 0) + Alpha- terpinolene	Gas phase	-96.883	-87.731	-94.052	6.321
	Aqueous phase	-2201.289	-585.391	-606.069	20.678
Iron (1 1 0) + Camphene	Gas phase	-72.722	-61.818	-62.648	0.829
	Aqueous phase	-2211.033	-595.135	-611.602	16.467
Iron (1 1 0) + Eucalyptol	Gas phase	-105.703	-63.766	-65.539	1.773
	Aqueous phase	-2215.922	-600.025	-622.598	22.574
Iron (1 1 0) + Gamma-cadinene	Gas phase	-144.103	-109.112	-117.146	8.034

Molecule	Phases	Total energy Kcal/mol	Adsorption energy kJ/mol	Rigid adsorption energy kJ/mol	Deformation energy kJ/mol
	Aqueous phase	-2186.226	-570.328	-586.975	16.647
Iron (1 1 0) + Gamma-terpinene	Gas phase	-99.928	-87.032	-88.000	0.967
	Aqueous phase	-2194.563	-578.665	-599.868	21.203
Iron (1 1 0) + Humulene	Gas phase	-120.833	-95.815	-104.969	9.153
	Aqueous phase	-2189.288	-573.390	-592.684	19.294
Iron (1 1 0) + Isoborneol	Gas phase	-68.092	-57.545	-58.674	1.129
	Aqueous phase	-2199.552	-583.654	-602.896	19.242
Iron (1 1 0) + Linalool	Gas phase	-127.168	-87.801	-90.464	2.663
	Aqueous phase	-2183.844	-567.946	-587.222	19.275
Iron (1 1 0) + O-cymene	Gas phase	-78.786	-74.047	-76.219	2.172
	Aqueous phase	-2195.270	-579.372	-601.810	22.437
Iron (1 1 0) + Terpinene-4-ol	Gas phase	-117.084	-87.512	-90.411	2,900
	Aqueous phase	-2192.474	-576.576	-600.552	23.976
Iron (1 1 0) + Terpineol	Gas phase	-134.073	-88.471	-90.444	1.973
	Aqueous phase	-2176.230	-560.332	-578.392	18.060
Iron (1 1 0) + Terpinolene	Gas phase	-97.904	-88.753	-95.092	6.339
	Aqueous phase	-2183.881	-567.983	-584.628	16.644
Iron (1 1 0) + Alpha-terpineol	Gas phase	-134.073	-88.471	-90.444	1.973
	Aqueous phase	-2176.230	-560.332	-578.392	18.060

Relatively to Table 10, which presents the Monte Carlo simulation results of various REO molecules adsorbed on the Fe(110) surface, it is evident that adsorption is much more favorable in the aqueous

phase compared to the gas phase. The more negative total and adsorption energies in aqueous H□SO□ confirm that the corrosive environment enhances the interaction of REO molecules with the metal surface.

In particular, molecules such as β-thujene, β-caryophyllene, α-terpinolene, camphene, and eucalyptol exhibit the most negative adsorption energies in the aqueous phase (–570 to − 600 kJ/mol), indicating stronger binding and greater potential as corrosion inhibitors. By contrast, molecules such as α-pinene, β-myrcene, and borneol acetate show comparatively weaker adsorption, though still more favorable than in the gas phase.

Rigid adsorption and deformation energies further support these observations. In the gas phase, deformation energies remain low, suggesting little structural rearrangement upon adsorption. However, in the aqueous phase, deformation energies increase notably (16–24 kJ/mol), showing that many REO molecules undergo structural adjustments to maximize stabilization at the Fe(110) surface.

In summary, the results highlight that REO molecules have a strong affinity for the Fe(110) surface in acidic aqueous environments. Among them, β-thujene, β-caryophyllene, α-terpinolene, and eucalyptol stand out as the most promising corrosion inhibitors due to their highly negative adsorption energies and their ability to adapt structurally to optimize adsorption. These findings suggest that REO constituents could provide effective surface protection for iron against acidic corrosion.

Conclusion

The present study demonstrates that rosemary essential oil is an efficient and sustainable corrosion inhibitor for low-alloy steel exposed to 1 M H_2SO_4. Gravimetric and electrochemical tests showed a substantial decrease in corrosion rate with increasing inhibitor concentration, with the optimum level obtained at 1.5 g/l. At this concentration, REO produced the highest charge-transfer resistance, the lowest corrosion current density, and a marked reduction in double-layer capacitance, confirming the formation of a stable and adherent protective layer. Temperature-dependent measurements revealed that the inhibitory effect remains significant even under thermal activation, indicating that the adsorbed film possesses good stability in aggressive conditions. Adsorption analysis demonstrated that the inhibitor follows a Langmuir-type isotherm, with a spontaneous and energetically favorable interaction between REO molecules and the steel surface. Computational studies further supported these observations by identifying oxygenated monoterpenes as the key contributors to inhibition, owing to their strong electron-donating ability and highly favorable adsorption energies on the Fe(110) surface.

Declarations

Ethics approval

Not applicable.

Consent to participate

Not applicable.

Consent to publish

Not applicable.

Competing interests

The authors declare no competing interests

Funding

No funding was received for this study

Author contributions

Wafaa Zriouel: conceptualization, methodology, software, writing-original draft, formal analysis, writing–review and editing and supervision. Hassan Mabrak: investigation, methodology, formal analysis, writing-review and editing. Mohammed Oubahou: investigation, formal analysis, writing-review and editing, project administration, and validation. Youssef Ghandi : investigation, software, formal analysis, writing- review and editing. Youssef Naimi: validation, investigation, data curation, supervision, project administration, conceptualization, writing- review and editing. Belkheir Hammouti : validation, investigation, data curation, supervision, project administration, conceptualization, writing- review and editing.

Acknowledgements

We would like to thank the different research groups for their contributions to the development of this study.

References

1. Al Jahdaly BA (2023) Rosmarinus officinalis extract as eco-friendly corrosion inhibitor for copper in 1 M nitric acid solution: Experimental and theoretical studies. Arab J Chem 16:104411. https://doi.org/10.1016/j.arabjc.2022.104411
2. Aoudj SE, Kouache A, Khelifa A, Boutoumi H, Moulay S, Feghoul A, Idir B (2022) Experimental and theoretical studies of *Inula viscosa* extract as a novel eco-friendly corrosion inhibitor for carbon steel in 1 M HCl. J Adhes Sci Technol 36:988–1016. https://doi.org/10.1080/01694243.2021.1956215
3. Aulicky R, Vendl T, Douda O, Pavela R, Stejskal V (2025) Insecticidal activity of rosemary essential oil against primary and secondary storage beetles in the presence and absence of grain. J Stored Prod Res 111:102498. https://doi.org/10.1016/j.jspr.2024.102498
4. Baharin K, Sais MG, Razak AFI, Sirat SS, Tajuddin AM, Kamarudin MSR, Dzulkifli NN (2025) Hirshfeld, surface analysis, DFT and corrosion inhibition mechanism of vanillin 4-

ethylthiosemicarbazone on mild steel in 1M HCl. Mor J Chem 13:80–105. https://doi.org/10.48317/IMIST.PRSM/morjchem-v13i1.50111

5. Bharati D, Engelberg D, Unluer C (2025) Characterisation of passive layer on steel immersed in MgO-SiO2 binder suspension solution. Corros Sci 255:113149. https://doi.org/10.1016/j.corsci.2025.113149
6. Brandt CCM, Lobo VS, Colombo KF, Wancura JHC, Oro CED, Oliveira JV (2023) Rosemary essential oil microemulsions as antimicrobial and antioxidant agent in tomato paste. Food Chem 2:100295. https://doi.org/10.1016/j.focha.2023.100295
7. Carmona Hernandez A, Sanchez R, Palacios-González E, Flores-Frías EA, Landa-Gómez AE, Mejía E, Espinoza Vazquez A, Orozco-Cruz R, Galvan-Martinez R (2025) Electrochemical characterization of CO2 corrosion inhibition of API X100 by a Gemini surfactant under static and dynamic conditions. Metals 15:918. https://doi.org/10.3390/met15080918
8. Charrad S, Alrashdi AA, Lee H-S, El Aoufir Y, Lgaz H, Satrani B, Ghanmi M, Aouane EM, Chaouch A (2022) Cupressus arizonica fruit essential oil: A novel green inhibitor for acid corrosion of carbon steel. Arab J Chem 15:103849
9. Cherrak K, El Massaoudi M, Outada H, Taleb M, Lgaz H, Zarrouk A, Radi S, Dafali A (2021) Electrochemical and theoretical performance of new synthetized pyrazole derivatives as promising corrosion inhibitors for mild steel in acid environment: Molecular structure effect on efficiency. J Mol Liq 342:117507. https://doi.org/10.1016/j.molliq.2021.117507
10. Delley BJ (2000) Chem Phys 113:7756–7764
11. Denisa-Ioana R, Matei E, Avramescu S-M (2025) Recent development of corrosion inhibitors: Types, mechanisms, electrochemical behavior, efficiency, and environmental impact. Technologies 13:103. https://doi.org/10.3390/technologies13030103
12. Dennington RD, II, Keith TA, Millam JM (2016) GaussView 6.0.16. Semichem, Inc., Shawnee Mission
13. Haque J, AlBlewi FF, Wan Nik WB, Ikhmal WMKWM, Quraishi MA, Rezki N, Aouad MR (2024) Triazole-bearing sulfonamide linkage: Synthesis, characterization, and investigation as a versatile corrosion inhibitor. J Mol Struct 1308:138100. https://doi.org/10.1016/j.molstruc.2024.138100
14. Kamarul Baharin N, FI SAISMG, Sirat A, Tajuddin SS, Mohd Kamarudin AM, Dzulkifli SR (2025) Hirshfeld, surface analysis, DFT and corrosion inhibition mechanism of vanillin 4-ethylthiosemicarbazoneon mild steel in 1M HCl. Mor J Chem 13:80–105. https://doi.org/10.48317/IMIST.PRSM/morjchem-v13i1.50111
15. Khan G, Basirun WJ, Badry ABM, Kazi SN, Ahmed P, Ahmed SM, Khan GM (2018) Corrosion inhibition performance and adsorption mechanism of novel quinazoline Schiff base on low alloy steel in HCl media. Int J Electrochem Sci 13:12420–12436. https://doi.org/10.12964/2018.12.40
16. Li W, Ma T, Tan B, Zhang S, Yan M, Ji J, Wang X, Wang F (2022) The effect of structural properties of benzo derivative on the inhibition performance for copper corrosion in alkaline medium: Experimental and theoretical investigations. Colloids Surf Physicochem Eng Asp 649:129531. https://doi.org/10.1016/j.colsurfa.2022.129531
17. Mahmoud GA, Abdel-Karim A, Ahmed SM, El-Meligi AA, El-Rashedy A (2025) Corrosion inhibition of copper alloy of archaeological artifacts in chloride salt solution using Aloe vera

green inhibitor. J Alloys Compd 1010:177540. https://doi.org/10.1016/j.jallcom.2024.177540

18. Mekha SR, Thomas R (2025) Surface-enhanced Raman spectroscopic sensing of the herbicide alachlor using Au16 nanocluster. Spectrochim Acta A 338:126132. https://doi.org/10.1016/j.saa.2025.126132
19. Nagarajan V, Bhuvaneswari R, Chandiramouli R (2023) Adsorption studies of camphene and eucalyptol molecules on orthorhombic germanane nanosheet – A first-principles investigation. J Mol Graph Model 119:108395
20. Nikhil K, Anunay P, Kumar S, Meena LK, Singh D (2026) An overview on emerging green organic corrosion inhibitors: sustainable solution for oil and gas industrial applications. RSC Adv 16:3909. https://doi.org/10.1039/d5ra08166a
21. Niu Y, Xu L, Qiao M, Wang Y (2025) The anti-depression effect and mechanism of harmonious rosemary essential oil and its application in microcapsules. Mater Today Bio 31:101546. https://doi.org/10.1016/j.mtbio.2025.101546
22. Okafor NA, Ume CS, Nnaji P, Iroha NB, Dagdag O, Ezeugo JO, Thakur A, Anadebe VC, Onukwul OD (2024) Physisorption or chemisorption: Insight from AI computing model based on DFT, MC/MD-simulation for prediction of MOF-based inhibitor adsorption on Cu in brine solution. Comput Theor Chem 1238:114730
23. Ou-Ani O, Zgueni H, Oucheikh L, Youssefi Y, Salah M, Matine A, Mabrouk EH, Oubair A, Chebabe D, Znini M (2025) Experimental and theoretical studies of the effect of *Ballota hirsuta* essential oil on carbon steel corrosion in a molar concentration of HCl. J Mol Struct 1332:141657. https://doi.org/10.1016/j.molstruc.2025.141657
24. Oubahou M, Zriouel W, Elbirgui K, Iounes N, El Guendouzi M, Naimi Y (2025) Comprehensive evaluation of lignin extracted from *Reseda luteola* L. waste: corrosion inhibition performance for XC48 carbon steel and ecotoxicological effect. Environ Sci Pollut Res 32:16229–16248. https://doi.org/10.1007/s11356-025-36667-y
25. Peköz R, Donadio D (2016) Effect of van der Waals interactions on the chemisorption and physisorption of phenol and phenoxy on metal surfaces. J Chem Phys 145:104701. https://doi.org/10.1063/1.4962236
26. Priya V, Bairagi H, Narang R, Shukla SK, Olasunkanmi LO, Ebenso E, Mangla B (2023) Experimental investigation of sustainable corrosion inhibitor albumin on low-carbon steel in 1N HCl and 1N H2SO4. Results Surf Interfaces 13:100155. https://doi.org/10.1016/j.rsurfi.2023.100155
27. Radek A (2009) Gaussian09, Gaussian, Inc, Wallingford CT, vol. 121, p. 150
28. Rajeev K, Chahal S, Kumar S, Lata S, Lgaz H, Salahi R, Jodeh S (2017) Corrosion inhibition performance of chromone-3-acrylic acid derivatives for low alloy steel with theoretical modeling and experimental aspects. J Mol Liq 243:439–450. https://doi.org/10.1016/j.molliq.2017.08.048
29. Suhartono T, Hazmatulhaq F, Sheng Y, Chaouiki A, Kamil MP, Ko YG (2024) In-situ construction of grass-like hybrid architecture responsible for extraordinary corrosion performance: Experimental and theoretical approach. Nano Mater Sci 4:44–59. https://doi.org/10.1016/j.nanoms.2023.05.004
30. Umoren SA, Ukashat M, Hernandez Santos J, Alnarabiji MS, Lim RC (2024) Investigations of corrosion inhibition of ethanolic extract of *Dillenia suffruticosa* leaves as a green corrosion

inhibitor of mild steel in hydrochloric acid medium. Corros Commun 15:52–62. https://doi.org/10.1016/j.corcom.2023.10.005

31. Yang J, Goksen G, Zhang W (2023) Rosemary essential oil: Chemical and biological properties, with emphasis on its delivery systems for food preservation. Food Control 154:110003. https://doi.org/10.1016/j.foodcont.2023.110003
32. Zarei Z, Kharaziha M, Karimzadeh F, Khadem E (2024) Synthesis and biological applications of nanocomposite hydrogels based on the methacrylation of hydroxypropyl methylcellulose and lignin loaded with alpha-pinene. Carbohydr Polym 346:122642
33. Zhao M, Zhang B, Li J, Zhang Q, Li H (2023) Molecular dynamics study on the diffusion behavior of water molecules and the dielectric constant of vegetable/mineral oil blends. Molecules 28:1067. https://doi.org/10.3390/molecules28031067
34. Zhou Y, Wang J, Wang X, Wang F, Li X (2023) Efficient production of α-pinene through identifying the rate-limiting enzymes and tailoring inactive terminal of pinene synthase in *Escherichia coli*. Fuel 343:127872
35. Zouarhi M (2023) Bibliographical synthesis on the corrosion and protection of archaeological iron by green inhibitors. Electrochem 4:103–122. https://doi.org/10.3390/electrochem4010010
36. Zriouel W, Belfadil D, Majid S, Hammouti B, Gmouh S (2026) Natural approaches to corrosion control: Essential oils as sustainable inhibitors. Int J Corros Scale Inhib 15:1–30. https://doi.org/10.17675/2305-6894-2026-15-1-1
37. Zriouel W, Mabrak H, Oubahou M, Bentis A, Hammouti B (2026) Rosemary essential oil as a sustainable corrosion inhibitor for copper: Quantum chemical insights, characterization, adsorption mechanisms applying Monte Carlo, and POM analysis. Turk Comp Theo Chem 10:79–100. https://doi.org/10.33435/tcandtc.1608380
38. Zriouel W, Mabrak H, Oubahou M, Naimi Y, Hammouti B (2025) Theoretical investigation of geranium essential oil compounds as green corrosion inhibitors for copper: Insights from DFT, Monte Carlo, and molecular dynamics simulations. ChemistrySelect 10:e02260. https://doi.org/10.1002/slct.202502260
39. Zriouel W, Oubahou M, Hammouti B (2025) Exploring geranium essential oil as a sustainable corrosion inhibitor for XC48 carbon steel in 1 M HCl. Int J Corros Scale Inhib 14:353–380. https://doi.org/10.17675/2305-6894-2025-14-1-22

Table 9

Table 9 is available in the Supplementary Files section.

Figures

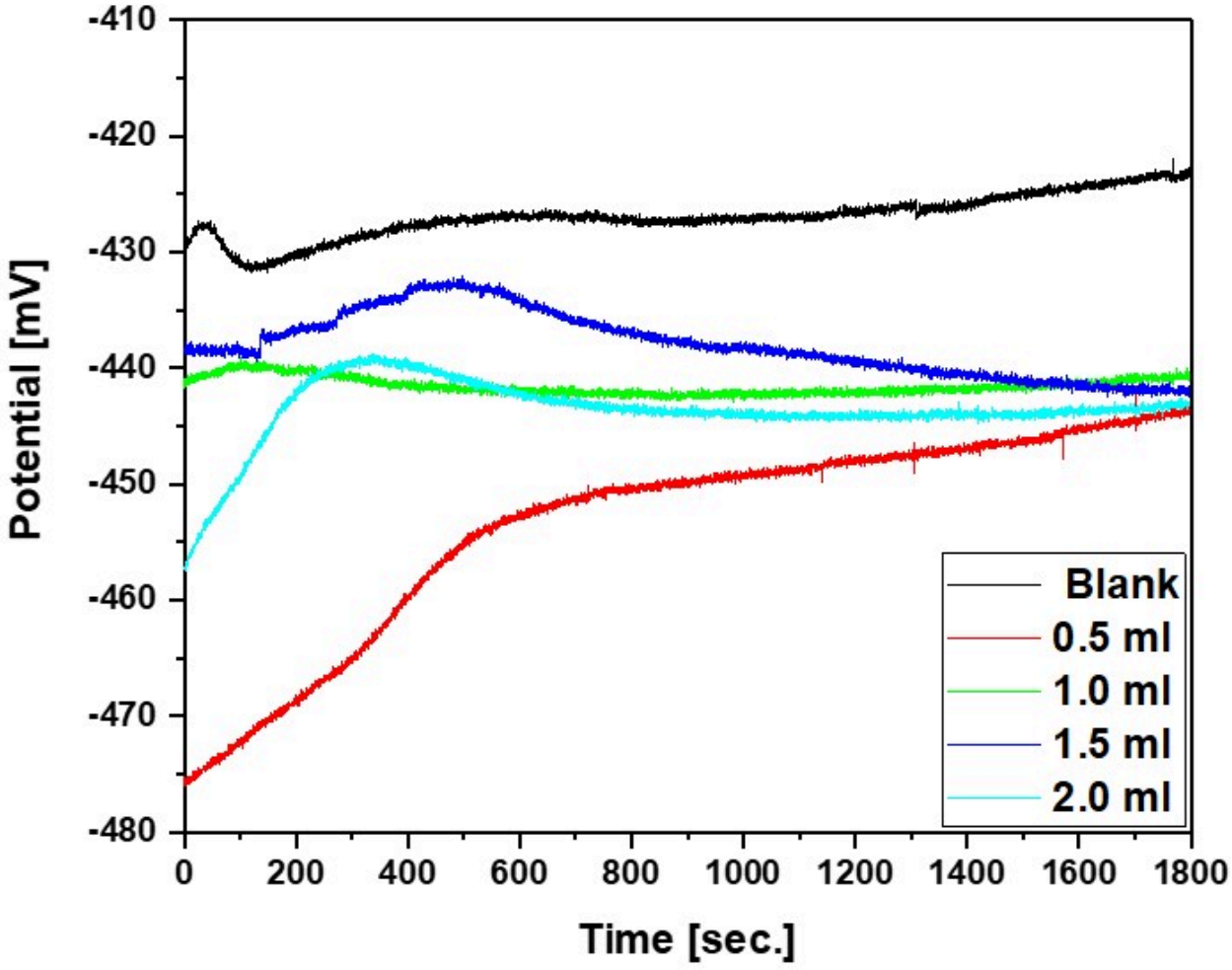


Figure 1

Evolution of the OCP of Low Alloy Steel immersed in 1 M H_2SO_4 in the absence and presence of REO at various concentrations

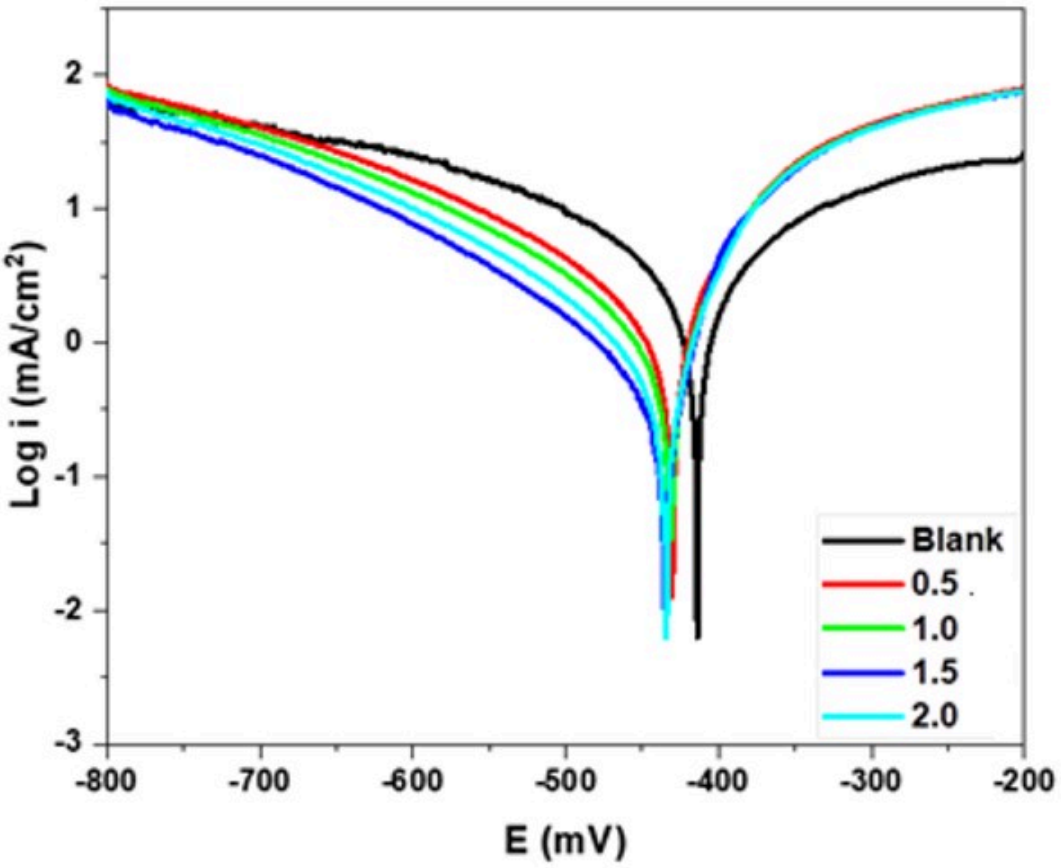


Figure 2

Potentiodynamic polarization curves of LAS immersed in sulphuric acid solution without and with the addition of REO at different concentrations 298 K.

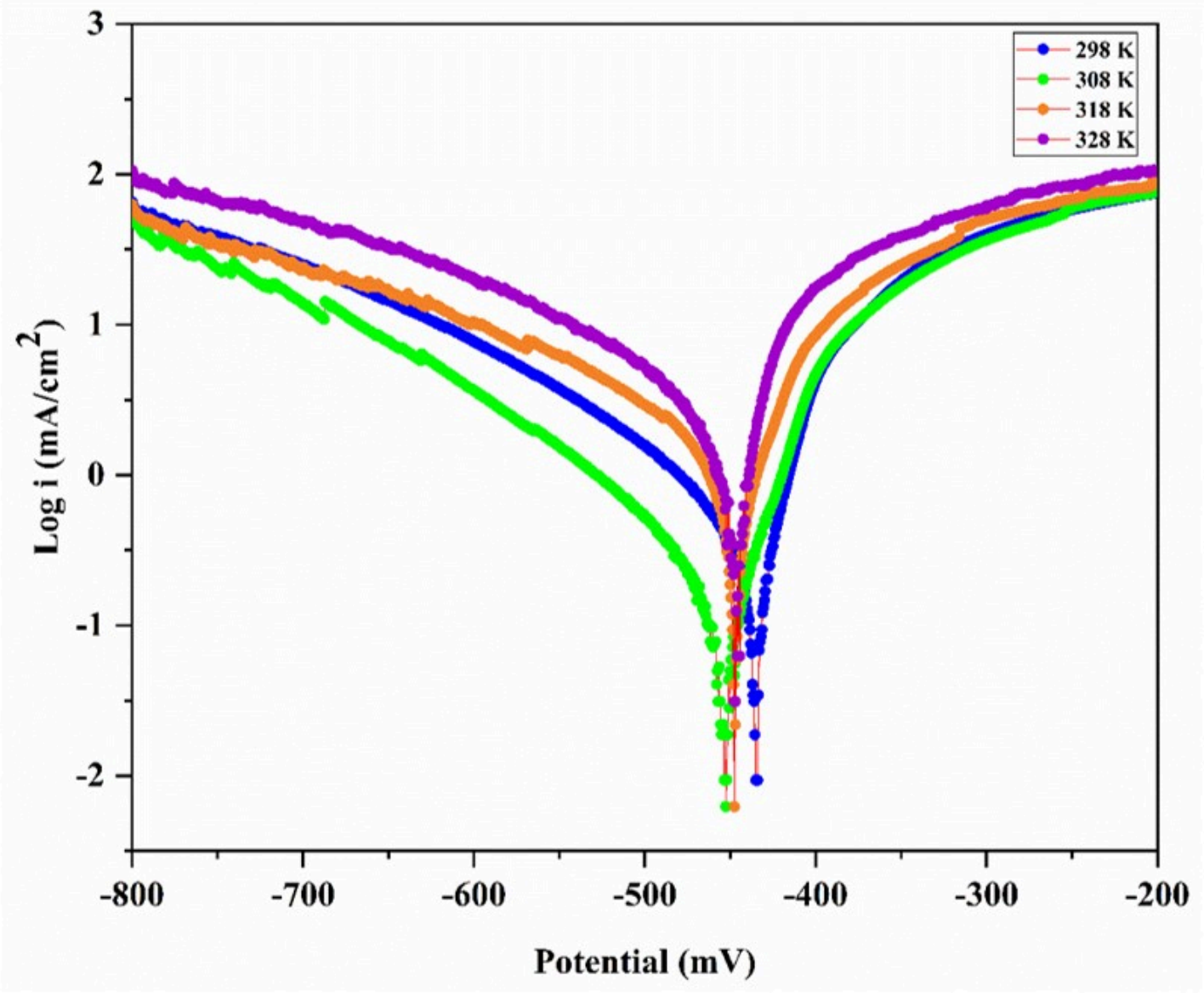


Figure 3

Polarization curves of carbon steel in H_2SO_4 with REO at various temperatures.

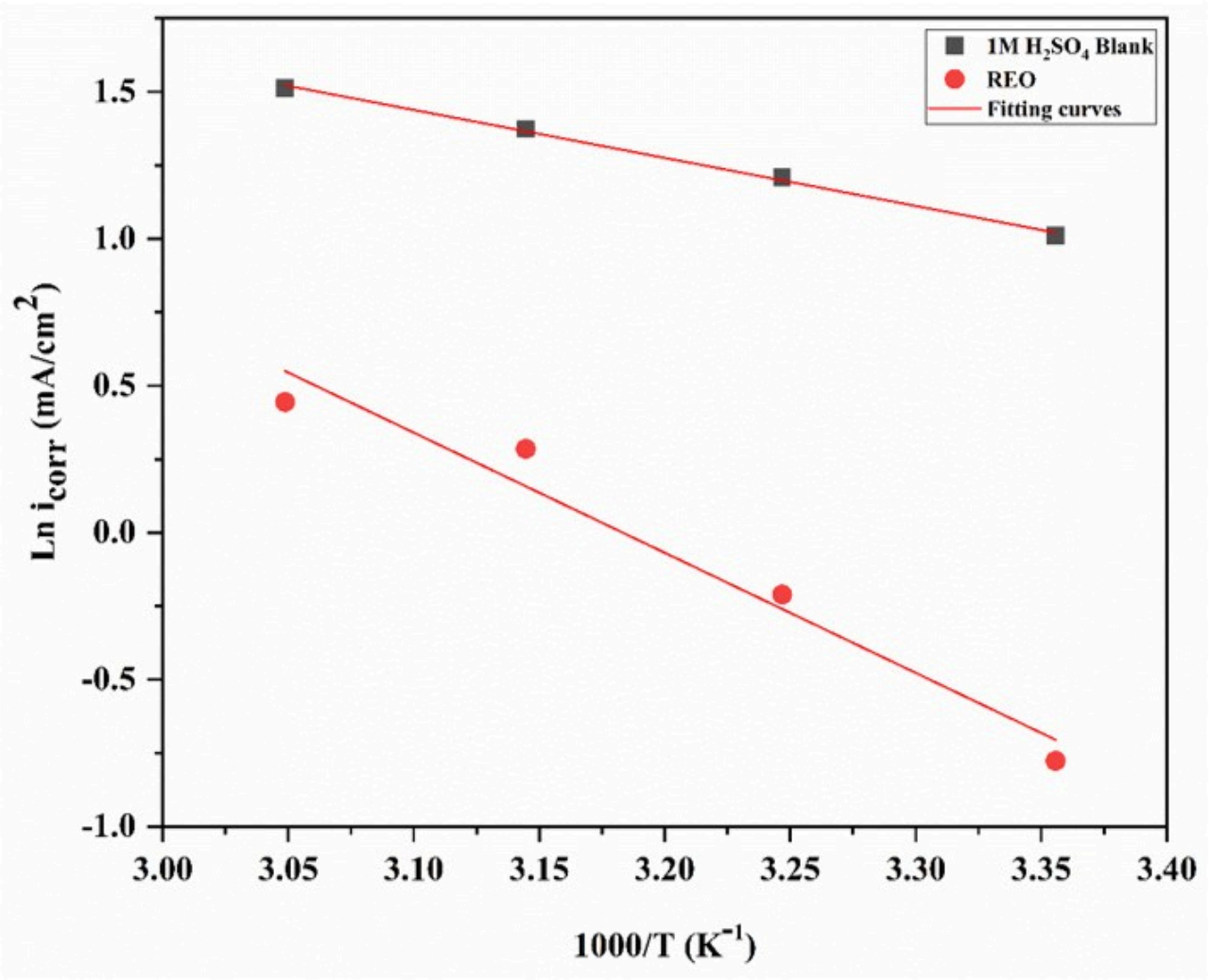


Figure 4

Arrhenius plots for LAS corrosion in 1 M H_2SO_4 with REO.

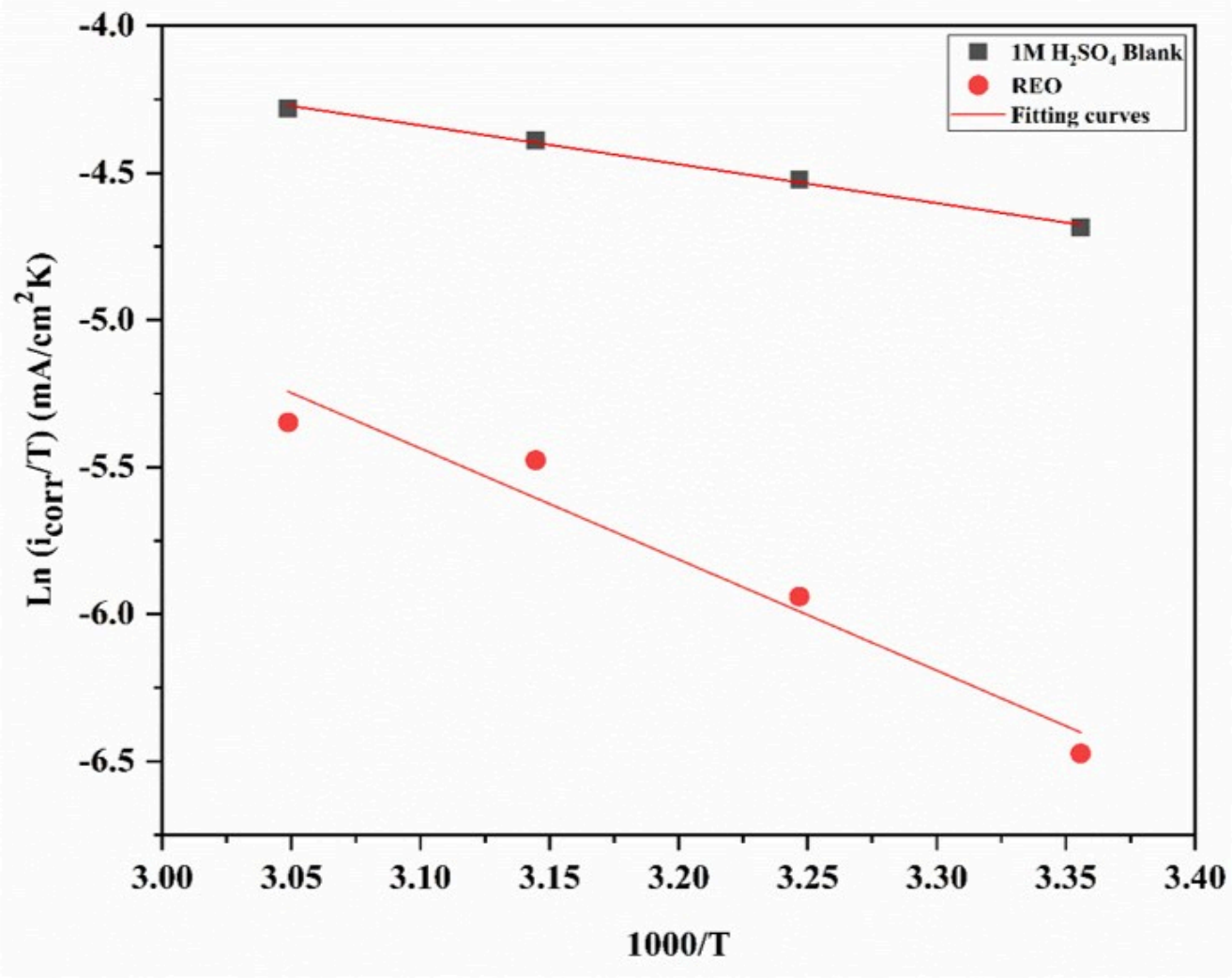


Figure 5

Transition-state plots for LAS in 1 M H_2SO_4 in the presence of REO.

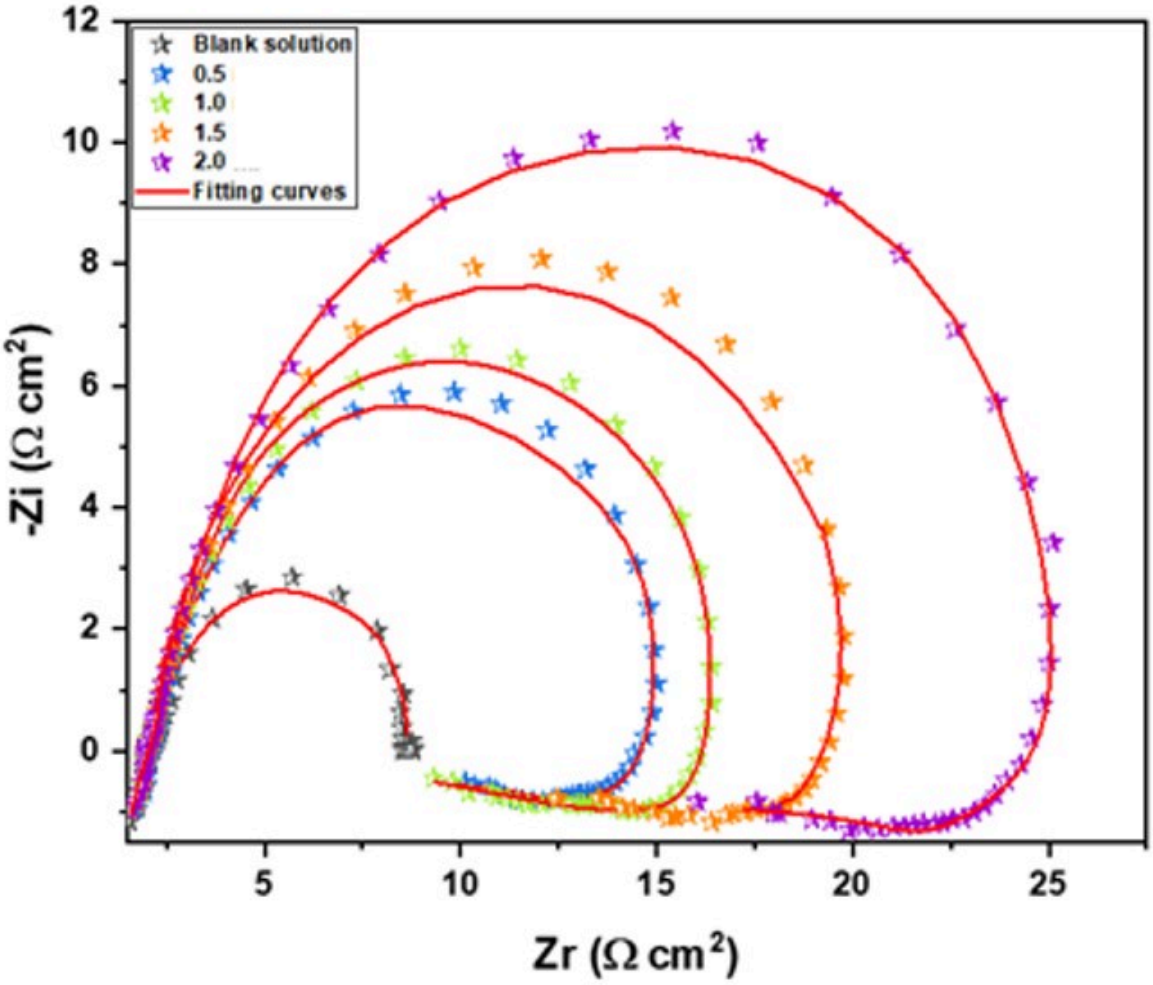


Figure 6

Impedance curves of LAS in 1 M H_2SO_4 without and with REO.

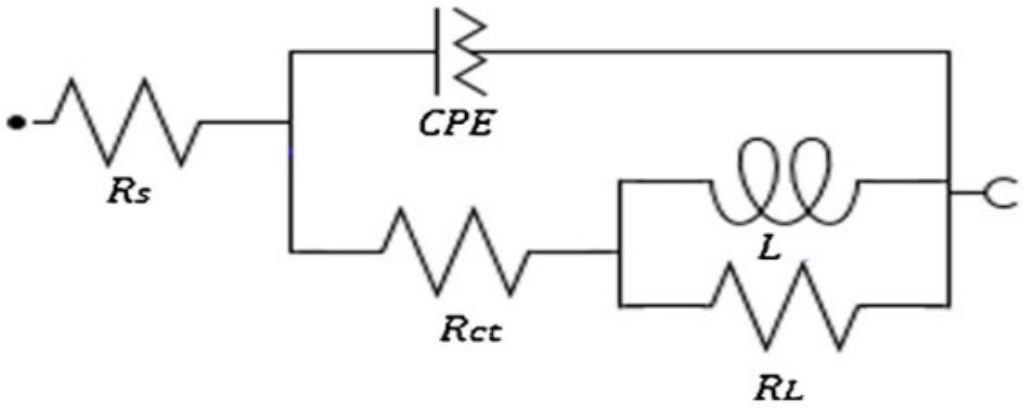


Figure 7

Equivalent circuit model representing the LAS/ H_2SO_4 system in the presence of REO

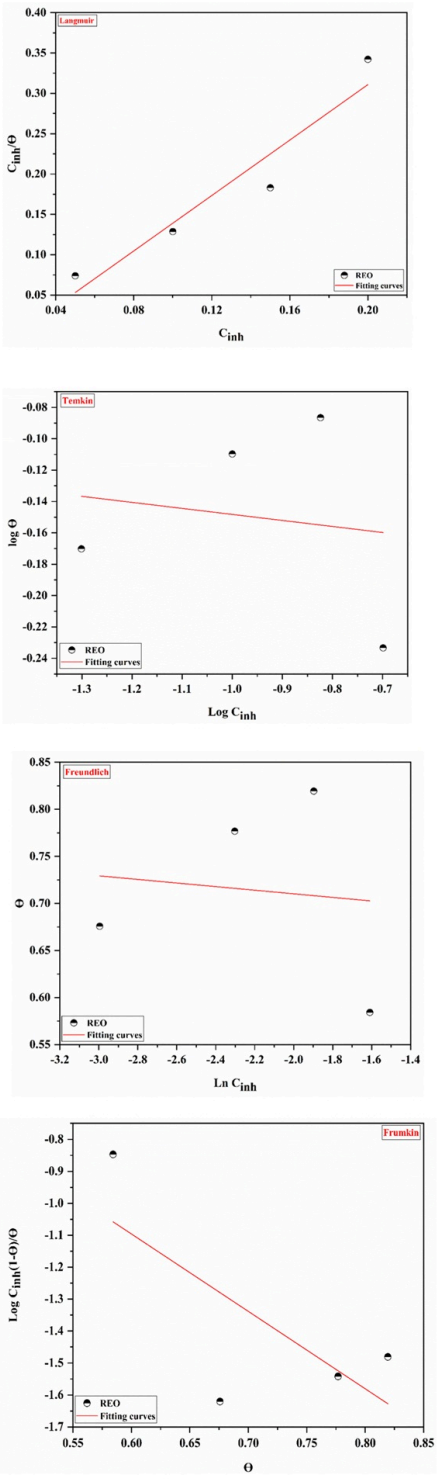


Figure 8

Figure 9. Comparison of Langmuir, Temkin, Freundlich, and Frumkin adsorption isotherm models describing the adsorption behavior of REO on LAS in 1 M H_2SO_4 solution.

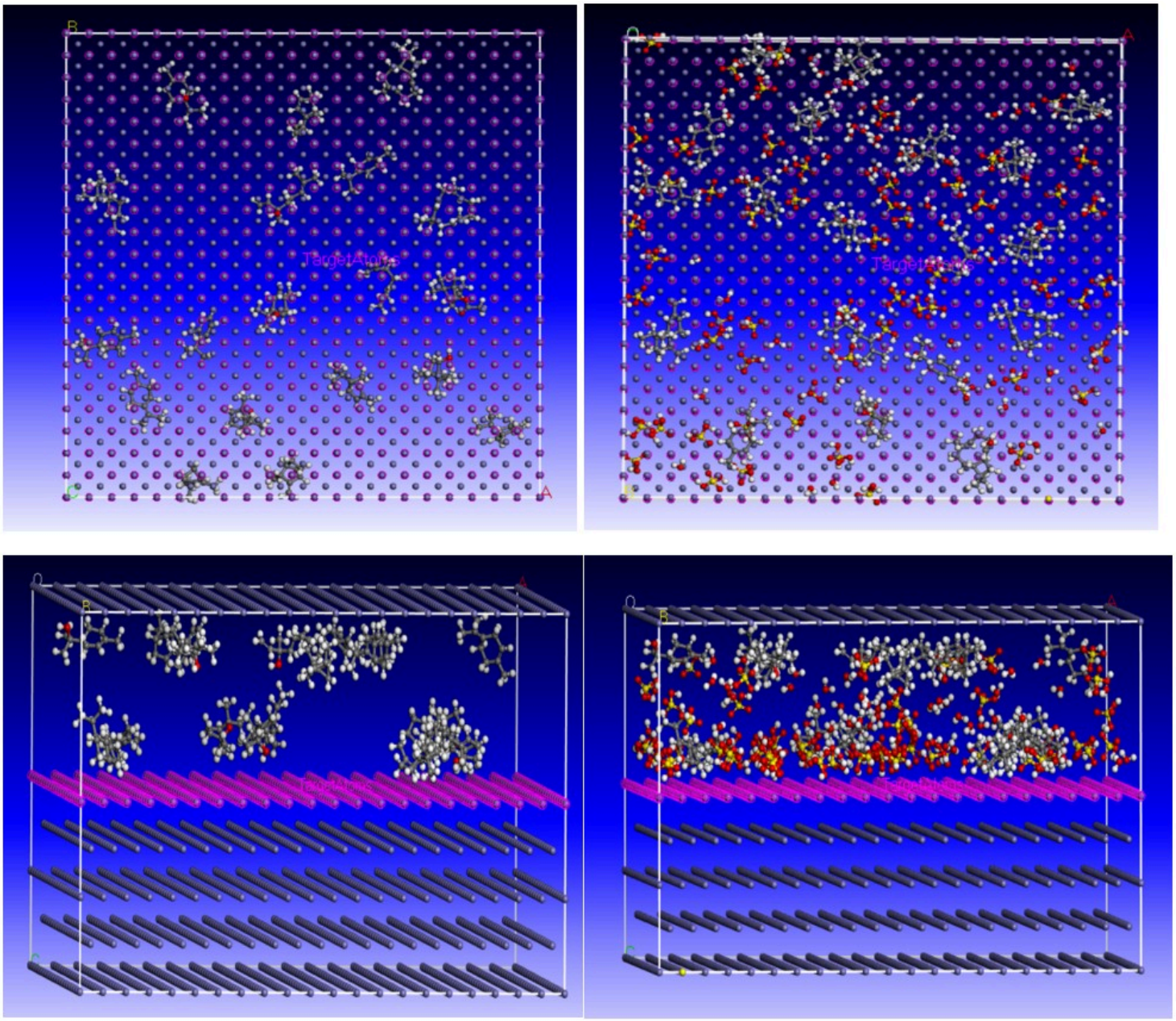


Figure 9

Figure 10. Top and side views of the Fe (1 1 0) surface with the adsorbed molecules.

Supplementary Files

This is a list of supplementary files associated with this preprint. Click to download.

- Table9.docx